



Modeling Internal Shorting Process in Large-Format Li-Ion Cells

Wei Zhao,^a Gang Luo,^b and Chao-Yang Wang^{a,b,*,z}

^aElectrochemical Engine Center (ECEC), Department of Mechanical and Nuclear Engineering, The Pennsylvania State University, University Park, Pennsylvania 16802, USA

^bEC Power, State College, Pennsylvania 16803, USA

Safety has become an increasingly pressing issue in large-format, energy-dense Li-ion batteries for automotive applications. Among various abusive scenarios for Li-ion batteries, internal short-circuit is most dangerous and has been the root cause for several highly publicized catastrophic accidents in recent years. Nail penetration and crush tests are commonly used as experimental proxy for internal shorting, but fail to truly emulate the internal short-circuits seen in field accidents. Also, experimental methods only give a simple pass/fail result, providing little insight into fundamental mechanisms governing the battery thermal and electrochemical response during internal shorting. In this study, a 3D electrochemical-thermal coupled model is used to scrutinize the internal short-circuit process in a large-format Li-ion cell with a stacked-electrode design. The model reveals the 3D electrochemical and thermal processes inside the battery cell during internal shorting. A parametric study is carried out, showing that the short-circuit resistance and the number of shorted electrode layers have the most significant influence on cell electrochemical and thermal behavior. Novel experimental methods, designed to precisely control these key parameters, must be developed in order to advance the understanding and improvement of Li-ion battery safety.

© The Author(s) 2015. Published by ECS. This is an open access article distributed under the terms of the Creative Commons Attribution 4.0 License (CC BY, <http://creativecommons.org/licenses/by/4.0/>), which permits unrestricted reuse of the work in any medium, provided the original work is properly cited. [DOI: 10.1149/2.1031507jes] All rights reserved.

Manuscript submitted February 2, 2015; revised manuscript received March 23, 2015. Published April 28, 2015.

As energy and power densities of Li-ion batteries rise ever higher to meet requirements of sustainable energy applications such as electric transportation and grid energy storage, risk of battery failure with potential for catastrophic incidents makes safety a primary concern. The highest specific energy available in today's commercial Li-ion rechargeable batteries is about 240 Wh/kg, almost 20% of the energy content of TNT at 4.61 MJ/kg.¹ Under normal discharge (charge), the chemical (electrical) energy is converted to electrical (chemical) energy with minimal heat generation. However, when the battery is exposed to abusive conditions, a large amount of heat could be generated due to unmanaged energy release or absorption. This increased heat generation will trigger a series of exothermic reactions that generate more heat, eventually leading to a thermal runaway. Catastrophic consequences will usually follow battery thermal runaway.

Internal short-circuit is the most common and dangerous abusive condition and is the cause of most field incidents involving Li-ion batteries. It occurs when a current path develops within the battery cell. It is usually caused as a result of manufacture defects or physical damages to the battery cell. The fundamental reason that internal short-circuit is so dangerous is that very high localized heating results from current flow through a short-circuit object (SCO). This localized heating is difficult to dissipate and the current flow is large, especially in large-format cells. The localized heating then triggers rapid temperature rise and thermal runaway of batteries. In addition, common protective devices installed externally on Li-ion batteries, such as positive temperature coefficient resistance (PTC), thermal and current fuses, pressure-release vent and battery management systems (BMS) are not able to protect the battery's internal shorting process.

Nail penetration and crush test are two commonly adopted experimental methods for internal short-circuit test of Li-ion cells. In a nail penetration test, a nail is forced to pierce the battery at a prescribed speed, inducing a short-circuit inside the cell. Heat is generated by current flowing through the cell and by current flowing through the nail. On the other hand, in a crush test, external force is applied to a crushing apparatus, such as a round bar or two flat layers. The sample battery within the crushing apparatus is then under the applied crushing force. Depending on the crushing force and method, different anode and cathode layers may be forced into contact with each other, causing internal short-circuit. The results of these tests have been documented in several articles in the literature.²⁻⁸

Although both tests are widely used, they have several limitations in terms of truly mimicking the internal short-circuit events in large-format Li-ion cells. First of all, large-format Li-ion cells are often constructed with multiple electrode layers. Both nail penetration test and crush test usually result in short-circuits in many electrode layers within a large-format cell. On the other hand, the internal short-circuit usually occurs with one or a few electrode layers, depending on the size of the SCO causing the short-circuit. As a result, the current flow path and heat generation distribution are very different from that in the nail penetration and crush tests. Figure 1a illustrates the current flow path in typical nail penetration and crush tests. Since most of the electrode layers are penetrated or crushed, it creates a short-circuit and closed current loop in each of the electrode layers. There is no or very little current flowing through the tabs from one electrode layer to another. The total heat generation is then distributed equally to each of the electrode layers, leading to a relatively global heating of the cell. Figure 1b shows the scenario commonly seen in a real internal short-circuit process, where a SCO is embedded within one electrode layer of the cell. The SCO could be a metal particle introduced during the cell manufacturing process. It can also be Li dendrite formed by Li plating due to overcharge or degradation. The SCO creates a short-circuit and current loop within the electrode layer where the SCO is located. This electrode layer not only discharges its energy to itself, it also serves as a load to the other electrode layers without a SCO inside. Hereafter, we call the former electrode layer "shorted" electrode layer and the latter "un-shortened" electrode layer. Because different electrode layers are connected by tabs, a large amount of current will be generated from un-shortened electrode layers, flow through the tabs, and converge to the shorted electrode layers and SCO. Therefore it can be deduced that not only will a hot spot exist around the SCO, but the temperature rise on the tabs will also be significant due to large current flow and small thermal mass of the tabs. Neither nail penetration or crush test, however, are capable of investigating these mechanisms. Secondly, both nail penetration and crush test are destructive tests. In these tests, the short-circuit process is usually accompanied by cell structure breach, electrolyte release and gas venting, which is not often seen in a field-failure involving internal short-circuit. These side effects are difficult to control and minimize which introduces complexity and reduces the reproducibility and reliability of the test results. Finally, the experimental studies only give simple pass/fail results and therefore provide few insights into the fundamental mechanisms, particularly the electrochemical and thermal coupling that governs the cell behavior during the internal short-circuit process.

In light of the limitation of test procedures, there is a need to utilize modelling tools to investigate the detailed fundamental mechanisms

*Electrochemical Society Active Member.

^zE-mail: cwx31@psu.edu

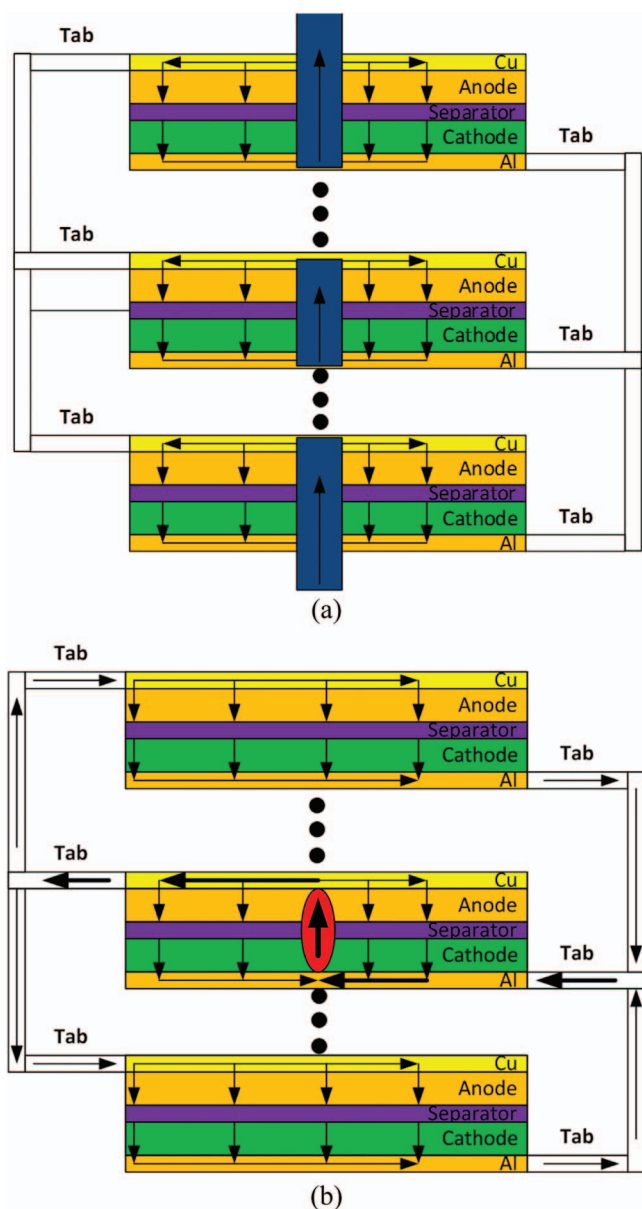


Figure 1. Difference of current flow path between (a) nail penetration and crush tests (b) internal short-circuit process.

of Li-ion cells during internal short-circuit process. Compared with experimental works, there are few efforts on the modelling of Li-ion battery safety and particularly internal short-circuit process. Most of the work in the literature focuses on predicting cell thermal response by exerting specific heat sources due to various exothermic reactions. Several of these modelling studies can be found in Refs. 7,9–12 and their findings were summarized in Ref. 13. In these studies, the coupling of cell electrochemical performance and thermal behavior during the internal short-circuit process, which determines the cell safety behavior, was not considered. Recently, there have been several modelling studies attempting to use a coupled electrochemical-thermal model to investigate the internal short-circuit process. Yamauchi et al.¹⁴ and Zavalis et al.¹⁵ used electrochemical-thermal model to simulate the internal short-circuit scenario, but the geometries for the cells in both studies were simplified and cannot represent realistic current flow and thermal conditions in typical large-format Li-ion cells. Santhanagopalan et al.¹⁶ presented an electrochemical-thermal coupled model to study the internal short-circuit with a real cell geometry. However, the electrochemical behavior of the cell during internal short-circuit, and how it connects to the cell's thermal behavior, was neither described nor illustrated with results. Fang et al.¹⁷ investigated internal short-circuit using a 3D electrochemical-thermal model. However, the results did not show any 3D results of current and temperature distribution in the cell geometry, which is of vital importance to advance the fundamental understanding of internal short-circuit process in large-format Li-ion cells.

In the present paper, we present a study to investigate the internal short-circuit process in a large-format Li-ion cell, for the first time in the literature, using a 3D electrochemical-thermal coupled model. We will demonstrate that the shorting resistance induced by the SCO and SCO size have significant effect on the cell electrochemical behavior and heating mechanisms during the internal short-circuit process.

Numerical Model

3D electrochemical-thermal coupled model.— A 3D electrochemical-thermal coupled model has been developed to study large-format Li-ion cells.¹⁸ The model was developed based on several popular Li-ion cell models in the literature,^{19–25} and has been validated extensively against experimental data on both small cells²⁶ and large-format cells.^{27–28} The governing equations of the model are listed in Table I and the detailed description of the model can be found in Ref. 18.

Internal short-circuit boundary condition.— In internal short-circuits, one or a few electrode layers are shorted by the SCO. There is a closed loop current formed within each of the shorted electrode layers. The other un-shortened electrode layers supply energy to the shorted

Table I. Governing equations of the 3D Li-ion cell model.

Conservation Equations:

$$\text{Charge, Solid Phase} \quad \nabla \cdot (\sigma^{eff} \nabla \phi_s) = j^{Li} \quad [1]$$

$$\text{Charge, Electrolyte Phase} \quad \nabla \cdot (k^{eff} \nabla \phi_e) + \nabla \cdot (k_D^{eff} \nabla \ln c_e) = -j^{Li} \quad [2]$$

$$\text{Species, Electrolyte Phase} \quad \frac{\partial(\epsilon_e c_e)}{\partial t} = \nabla \cdot (D_e^{eff} \nabla c_e) + \frac{1-t_0^+}{F} j^{Li} \quad [3]$$

$$\text{Species, Solid Phase} \quad \frac{\partial c_s}{\partial t} = \frac{D_s}{r^2} \frac{\partial}{\partial r} (r^2 \frac{\partial c_s}{\partial r}) \quad [4]$$

$$\text{Heat} \quad \frac{\partial(\rho c_p T)}{\partial t} = \nabla \cdot (k \nabla T) + q_e + q_r + q_j \quad [5]$$

$$j^{Li} = a_s i_0 \{ \exp[\frac{\alpha_a F}{RT} \eta] - \exp[-\frac{\alpha_c F}{RT} \eta] \} \quad [6]$$

$$\eta = \phi_s - \phi_e - U \quad [7]$$

$$i_0 = k(c_e)^{\alpha_a} (c_{s,max} - c_{s,e})^{\alpha_a} (c_{s,e})^{\alpha_c} \quad [8]$$

$$q_j = \sigma^{eff} \nabla \phi_s \nabla \phi_s + k^{eff} \nabla \phi_e \nabla \phi_e + k^{eff} \nabla \ln c_e \nabla \phi_e \quad [9]$$

$$q_r = j^{Li} (\phi_s - \phi_e - U_j) \quad [10]$$

$$q_e = j^{Li} (T \frac{\partial U_j}{\partial T}) \quad [11]$$

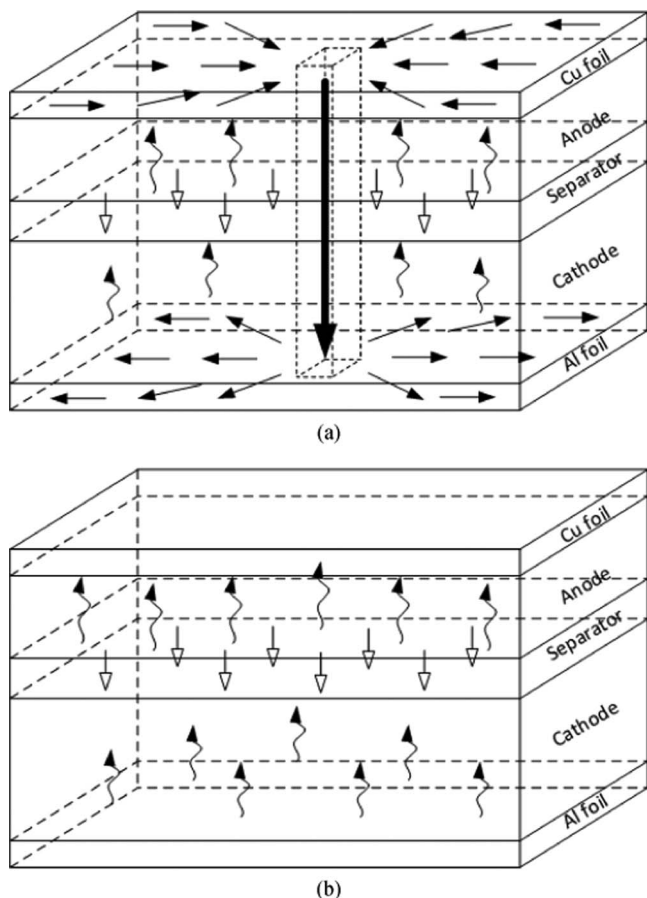


Figure 2. Schematic of the electrons and ions transport path during internal short-circuit process (a) shorted electrode layers and (b) un-shortened electrode layers.

electrode layers. The current flows through the tabs that connect the electrode layers from the un-shortened to the shorted electrode layers. This current flow path is illustrated in Figure 1b. Because of this 3D current flow, we cannot use only one electrode layer to represent the cell electrochemical performance as we did for the modelling of nail penetration process.¹³ All the electrode layers must be considered and meshed in the model. The tabs connecting the electrode layers are also meshed. The governing equations are solved on the full 3D cell geometry.

The internal short-circuit boundary condition is implemented in the same way as in Ref. 13. The electrons and ions flow paths within the shorted and un-shortened electrode layers are illustrated in Figure 2a and Figure 2b, respectively. It can be seen that the un-shortened electrode layer behaves like a normal discharge process and therefore does not need special treatment. The shorted electrode layer, on the other hand, has unique electron and ion transport paths. When the SCO is present in the shorted electrode layer, it internally connects the Cu foil and Al foil. The delithiation reaction occurs in the anode active materials releasing electrons and lithium ions. The electrons transport to the Cu foil and converge to the short-circuit spot. The electrons are further conducted through the SCO and spread out throughout the Al foil. The lithium ions, on the other hand, transport through the separator to the cathode. The lithiation reaction happens in the cathode active material with the lithium ions from the separator and electrons from the Al foil. Because the size of SCO is much smaller than the cell geometry, instead of explicitly solving the solid potential equation within the SCO body, a constant resistance boundary condition is applied on the surface of Al foil at the location of the short-circuit spot, as shown in Figure 3. A fixed voltage (usually 0) boundary condition is applied on the Cu surface at the location of short-circuit spot. In this way, the

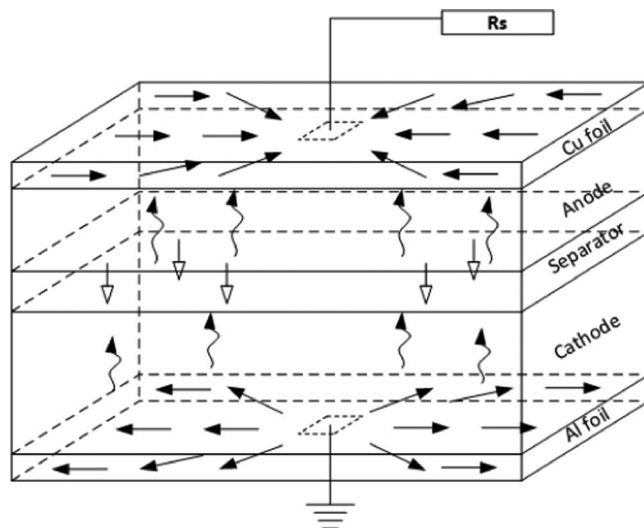


Figure 3. Schematic of applying constant resistance boundary condition at the short-circuit location.

electron and lithium ion transport paths in the shorted electrode layers are equivalent to those shown in Figure 2a, but the implementation is greatly simplified. The current flow between the shorted and un-shortened layers through the tabs will be automatically solved when the governing equations are solved on the 3D computational mesh.

The heat generation on the SCO due to current passing by is added onto the SCO body explicitly. The current passing through the SCO can be calculated using Ohm's law,

$$I_s = \frac{\Delta\phi_{s,p}}{R_s} \quad [12]$$

where $\Delta\phi_{s,p}$ is the solid potential drop along the SCO axial direction. R_s is the overall shorting resistance induced by SCO. The volumetric heat generation within the SCO body is then calculated using Joule's law,

$$q_s = \frac{I_s^2 R_s}{V_{SCO}} \quad [13]$$

where V_{SCO} is the volume of the SCO body inside the cell. This heat generation is added as a source term to the cell volume occupied by the SCO when solving the energy equation (i.e. Eq. 5).

Other boundary conditions.— The solid phase and electrolyte concentration distributions are prescribed at the beginning of simulation as initial conditions.

$$c_e = c_{e,0}, \quad c_s = c_{s,0} \quad [14]$$

Because the electrolyte is confined in the electrodes and separator, zero flux boundary conditions are applied for Eqs. 3 and 4 at the interface between the current collector and electrode.

$$\frac{\partial c_e}{\partial n} = 0, \quad \frac{\partial \phi_e}{\partial n} = 0 \quad [15]$$

At all other boundaries,

$$\frac{\partial \phi_s}{\partial n} = 0 \quad [16]$$

Convective heat transfer boundary condition is applied on the outer surface of the cell with a constant heat transfer coefficient of 0.002 W/cm²K and the ambient temperature and cell initial temperature both at 25°C.

Numerical procedures.— The governing equations are discretized using finite volume method (FVM) and solved along with their initial

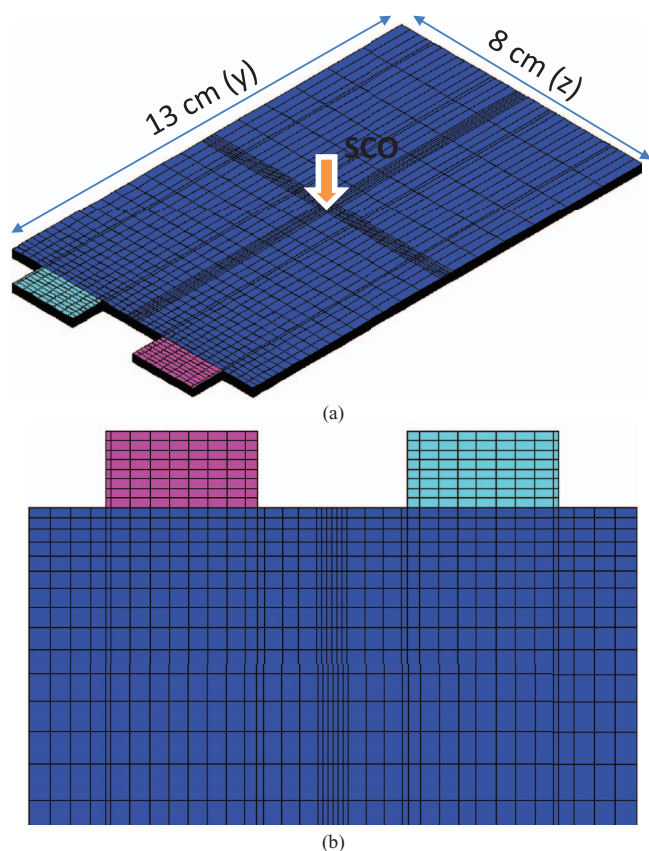


Figure 4. Geometry and computational mesh of the 5 Ah cell (a) overall mesh; (b) mesh around the tabs region.

and boundary conditions, using the user-coding capability of the commercial computational fluid dynamics (CFD) package, STAR-CD. All the equations are solved sequentially at each time step and the calculation proceeds to the next time step if the convergence criteria are met. For shorting condition, the residual of shorting current is used as a critical convergence criterion.

$$\varepsilon_I = \min \left(\left| \frac{I_a - I'_s}{I_s^0} \right|, \left| \frac{I_c - I'_s}{I_s^0} \right| \right) \theta \quad [17]$$

Table II. Design parameters for the 5Ah cell.

	Positive electrode	Negative electrode
Chemistry	$Li_yCo_{1/3}Ni_{1/3}Mn_{1/3}O_2$	Li_xC_6
Loading amount	12.5 mg/cm ²	6.05 mg/cm ²
Electrode thickness	78 μm	82 μm
Electrode height	13 cm	13 cm
Electrode width	8 cm	8 cm
Foil thickness	15 μm	8 μm
Separator thickness	20 μm	
Electrolyte	PC-EC-DMC 1.0 M LiPF ₆	
NP ratio	1.14	
No. of layers	26	
Total active area	2704 cm ²	
Nominal capacity	5 Ah	

where I_a and I_c are the total output current of anode and cathode electrode, respectively.

$$I_a = \int_{V, anode} j^{Li} dV \quad [18]$$

$$I_c = \int_{V, cathode} j^{Li} dV \quad [19]$$

And I_s^0 is the solution of the shorting current for the previous iteration. ε_I is chosen to be sufficiently small ($< 1.0 \times 10^{-6}$) to ensure converged results.

The Li-ion cell under study has a graphite based anode and NCM based cathode. The cell nominal capacity is 5 Ah. Figure 4 illustrates the computational mesh of the cell. The cell is 13 cm in height (y-dir) and 8 cm in width (z-dir). It consists of 26 electrode layers, stacked together in the cell thickness direction (x-dir). The total cell thickness is 2.6 cm. Each layer has a Cu foil, an anode electrode, a separator, a cathode electrode, and an Al foil. The Cu and Al foils are coated on both sides with anode and cathode materials, respectively. The tabs are welded outward on foils at the top edge of the cell and are clamped together. Heat conduction is allowed between welded tabs. The anode and cathode tabs have the same size, which is 2 cm in width and 1 cm in height. Other design parameters of the cell are listed in Table II. The physiochemical parameters used in the model are listed in Table III.

For all simulation cases, the SCO has an area of 4 mm × 4 mm and is embedded inside of the cell at the center of y-z plane. The SCO may short only one electrode layer, or it may cause several layers to be shorted, depending on the length of the SCO. Due to the possible large potential and temperature gradient, the mesh for the tabs and the

Table III. Physiochemical parameters used in the Li-ion battery model.

Parameter	Unit	Cu foil	Negative electrode	Separator	Positive electrode	Al foil
Density	kg/cm ³	8960×10^{-6}	1200×10^{-6}	525×10^{-6}	2860×10^{-6}	2700×10^{-6}
Specific heat	J/Kg K	385	1150	2050	1150	897
Thermal conductivity	W/cm K	3.95	0.004	0.005	0.004	2.4
Electron conductivity	S/cm	5.8×10^5	1.0		0.1	3.538×10^5
Maximum Li capacity	mol/cm ³		0.031		0.0518	
Stoichiometry at 0%/100% SOC			0.042/1.0		0.98/0.39	
Charge transfer coefficient			0.5		0.5	
Reference exchange current density	A/m ²		26		4.0	
Diffusion coefficient – solid phase	cm ² /s		9.0×10^{-10}		1.5×10^{-10}	
Bruggeman tortuosity exponent			1.5	1.5	1.5	
Transference number				0.363		
Porosity			0.27		0.32	
Thickness	cm	10×10^{-4}	74×10^{-4}	20×10^{-4}	63×10^{-4}	20×10^{-4}
Particle radius	cm		10×10^{-4}		3×10^{-4}	
Initial electrolyte concentration	mol/cm ³			0.001		
Heat transfer coefficient	W/cm ² K			0.002		

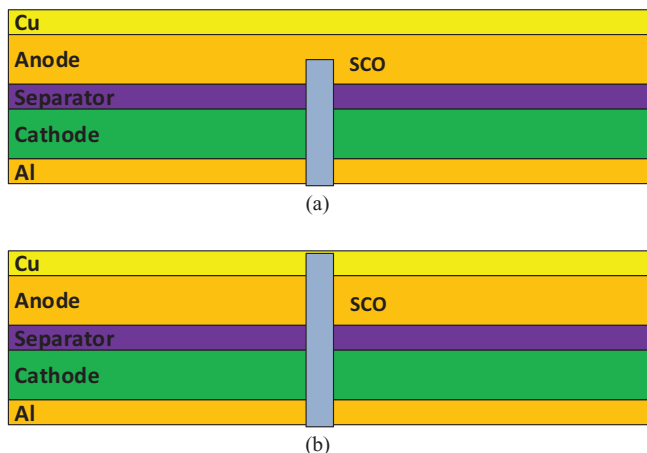


Figure 5. Two typical internal short-circuit scenarios (a) short between anode material and Al foil ($R_s = 4 \Omega/\text{layer}$); (b) short between Cu foil and Al foil ($R_s = 5.2 \text{ m}\Omega/\text{layer}$).

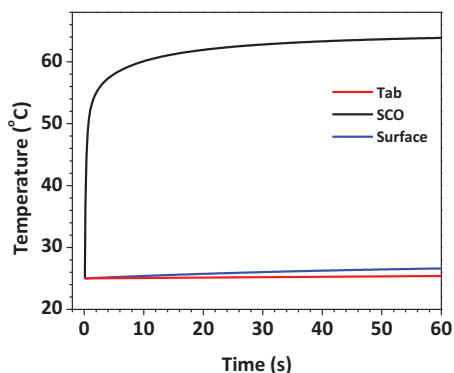


Figure 6. Temperature response (shorted layer = 13th layer, $R_s = 4 \Omega/\text{layer}$).

cell region around the tabs is refined, as shown in Figure 4b. The total mesh number is 595488. The Al tab temperature is monitored in the simulation. Cell surface temperature and SCO temperature are also monitored.

Results and Discussion

Effect of shorting resistance.— Shorting resistance has a significant influence on cell electrochemical and thermal behavior during short-circuit process. Determination of its value, however, is complicated by several parameters, including the intrinsic resistance of the SCO, the contact parameters between the SCO and cell, and the short-circuit scenarios. According to several studies^{16,29} there are four possible internal short-circuit scenarios: (i) the short between two current foils, (ii) the short between Al foil and anode active material, (iii) the short between Cu foil and cathode active material, (iv) the short between anode and cathode active material. To date, accurate value of the short-circuit resistance under various short-circuit scenarios cannot be measured in-situ due to the limitation of experimental techniques. In the present study, two estimated values of short-circuit resistance are chosen to represent two different short-circuit scenarios. As shown in Figure 5, in the first scenario, the short-circuit is caused by the SCO connecting the anode active material and Al foil. The estimated resistance is 4Ω per electrode layer. In the second scenario, Cu foil and Al foil are connected by the SCO. The estimated resistance is $5.2 \text{ m}\Omega$ per electrode layer. The shorted electrode layer is the 13th layer, counting from the bottom of the cell. Hence, the SCO is located approximately at the center of the cell thickness direction.

Figure 6 shows the calculated temperature profile for the large short-circuit resistance case ($R_s = 4.0 \Omega/\text{layer}$). The SCO temperature rises from the initial temperature of 25°C to above 60°C in about 20 s. On the other hand, the tab temperature and cell surface temperature remain low and increase slowly throughout the short-circuit period. The large difference between the SCO temperature and cell surface temperature implies localized heating on the SCO. Figure 7 illustrates contours of the surface temperature and the temperature at the center plane of the cell thickness direction. It can be seen that a hot spot

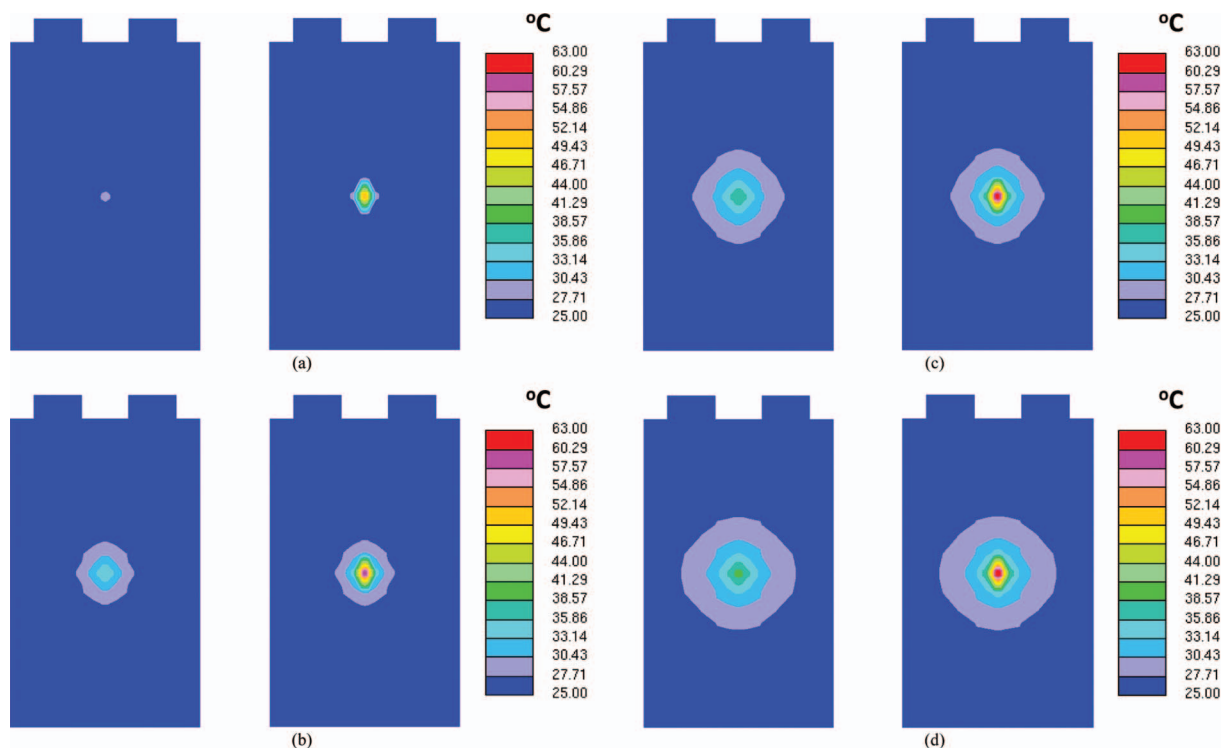


Figure 7. 2D temperature contour (shorted layer = 13th layer, $R_s = 4 \Omega/\text{layer}$, left: cell surface, right: cell center plane) (a) 1 s; (b) 10 s; (c) 30 s; (d) 60 s.

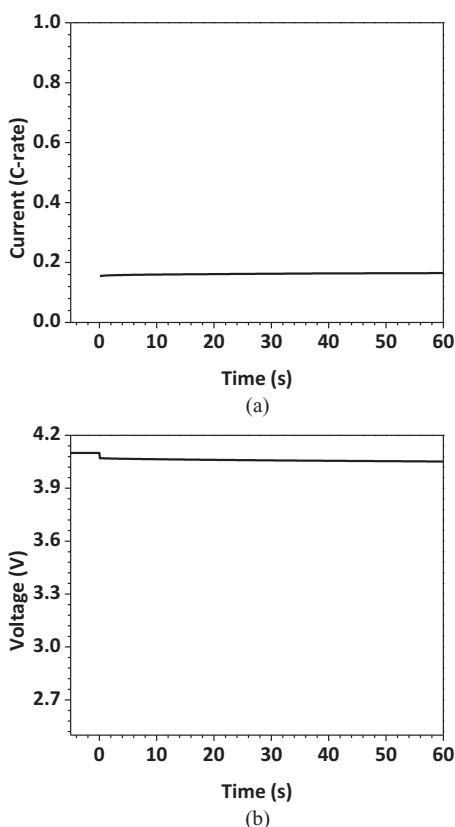


Figure 8. Current and voltage response (shorted layer = 13th layer, $R_s = 4 \Omega/\text{layer}$) (a) current; (b) voltage.

is formed and confined in the small region around the SCO. The temperature in the majority part of the cell, including the cell surface and tabs, remains low throughout the simulation period. This highly non-uniform temperature distribution is a result of localized heating on the SCO. The hot spot embedded deeply inside the cell makes it difficult for battery management systems (BMS) to provide early detection of short-circuit since only the cell surface temperature can be measured in a battery system.

The cell thermal response during the short-circuit process is governed by the electrochemical behavior of the cell. Figure 8 illustrates the current and voltage response during the short-circuit period. The short-circuit current is small and remains almost constant during the short-circuit process. The cell voltage decreases only slightly from the open-circuit voltage (OCV). Because the SCO resistance is much larger than cell internal resistance, the short-circuit current is controlled by the SCO resistance and the SCO draws most of the voltage drop. As a result, the total heat generation in cell is mainly contributed from the Joule heating on the SCO. The heat generation from the various internal processes of the cell, on the other hand, is negligible. The Li^+ concentration distribution in the electrolyte (Figure 9) and solid particles (Figure 10) varies only slightly from the initial conditions during the short-circuit period and hence has negligible effect on the thermal behavior.

Figure 11 illustrates the temperature profile of the small SCO resistance case ($R_s = 5.2 \text{ m}\Omega/\text{layer}$). The temperature behavior is significantly different from that of the large resistance case. The temperatures in both SCO and Al tab jump to above 500°C immediately following the short-circuit. Therefore, in contrast to the large resistance case, two hot spots are formed, one on the tabs and the other on the SCO. Because only the 13th layer is shorted by the SCO, current supplied from the other 25 layers will converge and pass through the Al and Cu tabs on the 13th layer. The small SCO resistance results in a large shorting current that in turn results in a large Ohmic heating

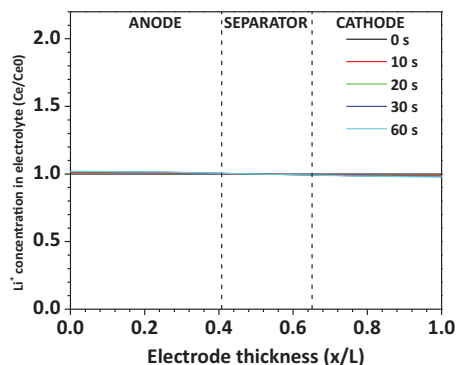


Figure 9. Li^+ concentration in electrolyte (shorted layer = 13th layer, $R_s = 4 \Omega/\text{layer}$).

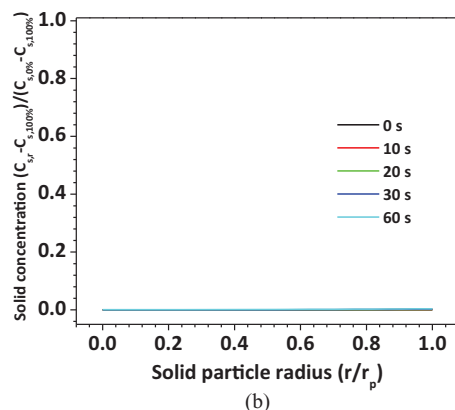
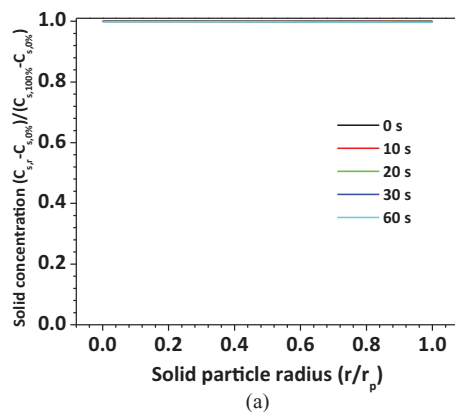


Figure 10. Li^+ concentration in active material particles (shorted layer = 13th layer, $R_s = 4 \Omega/\text{layer}$) (a) anode particle; (b) cathode particle.

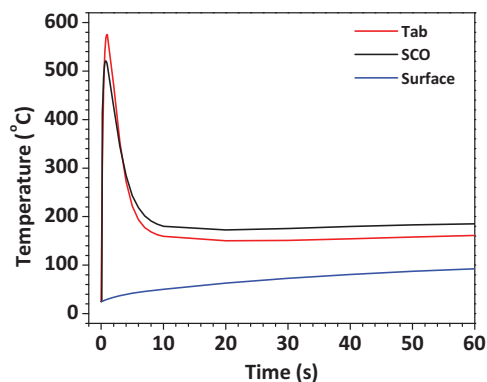


Figure 11. Temperature response (shorted layer = 13th layer, $R_s = 5.2 \text{ m}\Omega/\text{layer}$).

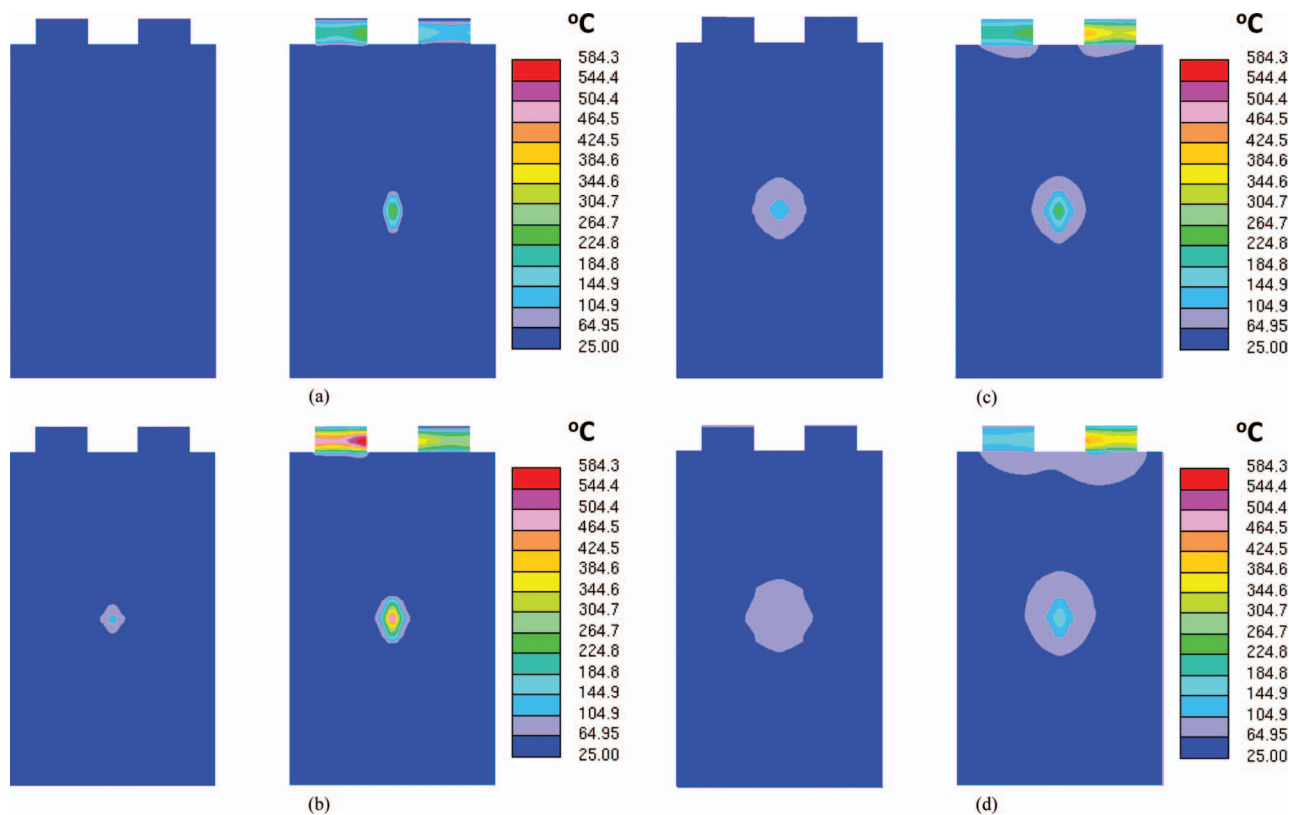


Figure 12. 2D temperature contour (shorted layer = 13th layer, $R_s = 5.2$ m Ω /layer, left: cell surface, right: cell center plane) (a) 0.1 s; (b) 1 s; (c) 5 s; (d) 10 s.

on the tabs. Also, because the tabs are very small (their thickness is the same as the foils), a sharp temperature rise is caused due to their small thermal mass.

From the cell temperature contour shown in Figure 12, it can be seen that the heating is localized around the SCO, and on the two current collecting tabs of the 13th electrode layer as well. The temperature in these areas rises to $\sim 600^\circ\text{C}$ in only 1 s after the short-circuit. Exothermic reactions are inevitable and may trigger thermal runaway.

The electrochemical behavior of the small resistance case is also vastly different from the large resistance case. As shown in Figure 13, the cell voltage drops to 2.2 V upon the start of short-circuit and decays exponentially thereafter. The inrush current amounts to 29 C-rate and also decays exponentially in the following short-circuit process. The decay of the short-circuit current and cell voltage implies mass transport limitation inside the cell. By checking the Li^+ concentration distribution in the electrolyte (Figure 14) and in the active material particles (Figure 15), we can find that the solid diffusion process is not the limiting factor since neither anode nor cathode solid particle reaches mass transport limitation. On the other hand, the Li^+ concentration distribution in the electrolyte shows that mass transport limitation occurs in the cathode electrode. The Li^+ concentration in the cathode drops quickly and becomes depleted in about 20 s. Because both the exchange current density i_0 and electrolyte conductivity κ^{eff} decrease as the depletion of Li^+ concentration in electrolyte,¹⁸ the cell internal resistance will increase significantly when the Li^+ depletion occurs. The increased cell resistance is the reason for the rapid decrease of shorting current and cell voltage.

Figure 16 and Figure 17 display the solid potential distribution and current flow vectors on the current collector foils. To better illustrate the result, the Cu and Al foils are spread out in a 2-D plane. The calculation data is then mapped onto the 2-D geometry. From Figure 16a and Figure 17a, it can be seen that the current is distributed from

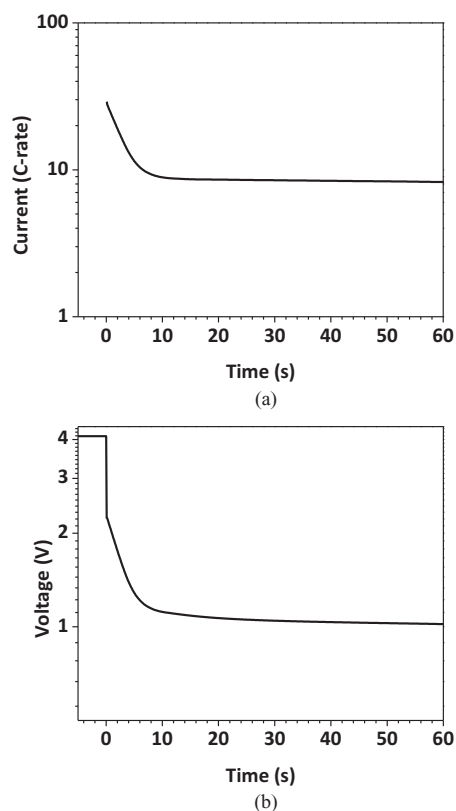


Figure 13. Current and voltage response (shorted layer = 13th layer, $R_s = 5.2$ m Ω /layer) (a) current; (b) voltage.

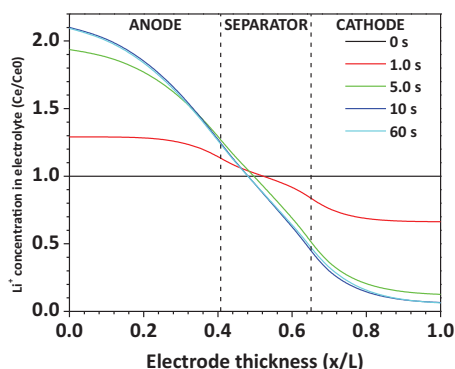


Figure 14. Li^+ concentration in electrolyte (shorted layer = 13th layer, $R_s = 5.2 \text{ m}\Omega/\text{layer}$).

the shorted electrode layer to the un-shortened layers at anode, as shown by the current flow vectors on the Cu foils. On the other hand, the current converges from the un-shortened electrode layers to the shorted electrode layers at cathode, as shown by the current vectors on the Al foils in Figure 16b and Figure 17b. The solid potential distribution of the small shorting resistance case indicates there is a large voltage gradient across the tabs of the shorted electrode layer, which explains the significant heating of tabs. For the large shorting resistance case, the voltage drop on foils and tabs is very small; most of the voltage drop is located in the SCO.

The single-layer shorting can best simulate the internal short-circuits seen in field incidents because internal short-circuits are usually caused by small metal particles that can only cause shorting of one single electrode layer. The above simulation shows that local heating

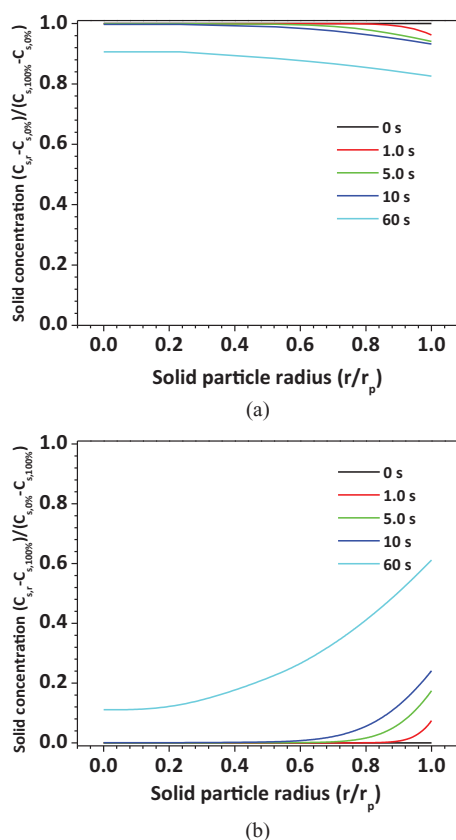


Figure 15. Li^+ concentration in active material particles (shorted layer = 13th layer, $R_s = 5.2 \text{ m}\Omega/\text{layer}$) (a) anode particle; (b) cathode particle.

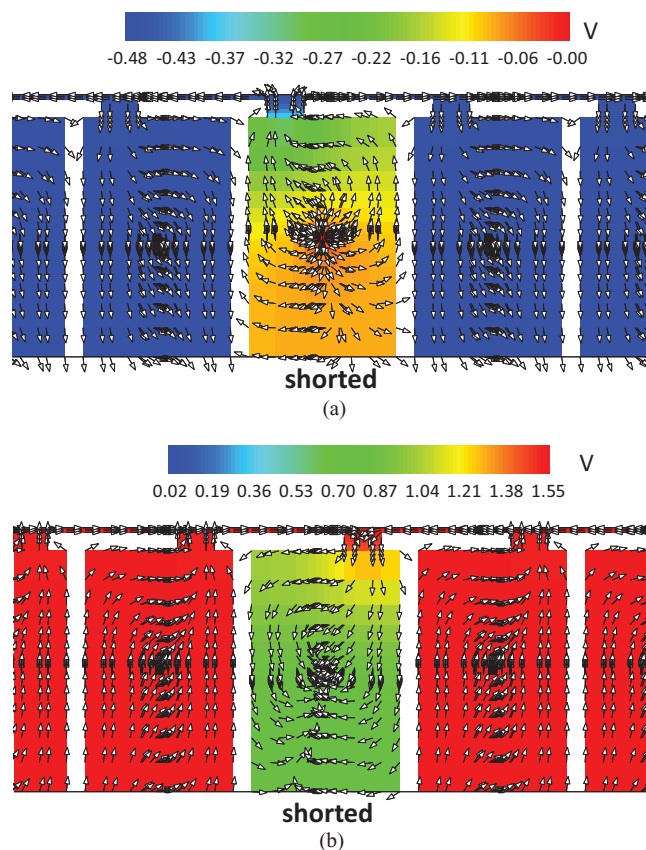


Figure 16. Solid potential and current flow vectors on the foils (shorted layer = 13th layer, $R_s = 5.2 \text{ m}\Omega/\text{layer}$) (a) Cu foil; (b) Al foil.

will always be caused in single-layer shorting. Besides heating on the SCO, significant temperature rise could also occur on the tabs. Therefore, in large format Li-ion cells, tabs temperature should be monitored for the detection of internal short-circuit.

Effect of number of shorted electrode layers.— The above cases investigate the short-circuit scenario when only one electrode layer among the 26 layers is shorted by the SCO. However, in some cases multiple electrode layers can be shorted. For example, when the cell is crushed or dented by external forces, more than one electrode layer can be shorted as a result of deformation of the cell structure. Lithium metal dendrite caused by lithium plating during overcharge may also grow large enough to penetrate through multiple electrode layers, causing multiple short-circuits. Therefore it is interesting to explore the difference in the behavior between single-layer shorting and multiple-layer shorting. The previous section studies the single-layer shorting where the 13th electrode layer is shorted by the SCO. In this section, the number of shorted electrode layer ranges from 2 to 26 and each shorted layer has identical shorting resistance. Because the 26 electrode layers are connected in parallel, the total resistance of N-layer shorting should equals 1/N of the shoring resistance for single-layer shorting, i.e.

$$R_{s,N\text{-layer}} = \frac{R_{s,1\text{-layer}}}{N} \quad [20]$$

Figure 18 and Figure 19 display the calculated temperature rise of Al tab and SCO during the simulated internal short-circuit period. For the small resistance case, as shown in Figure 18a, the temperature rise of both Al tab and SCO reduces as the increase of the number of shorted electrode layers. The reason is that for small shorting resistance, the shorting current is mostly determined by the cell internal processes. When multiple electrode layers are shorted, the total heat generation will be distributed to multiple tabs and SCOs, leading

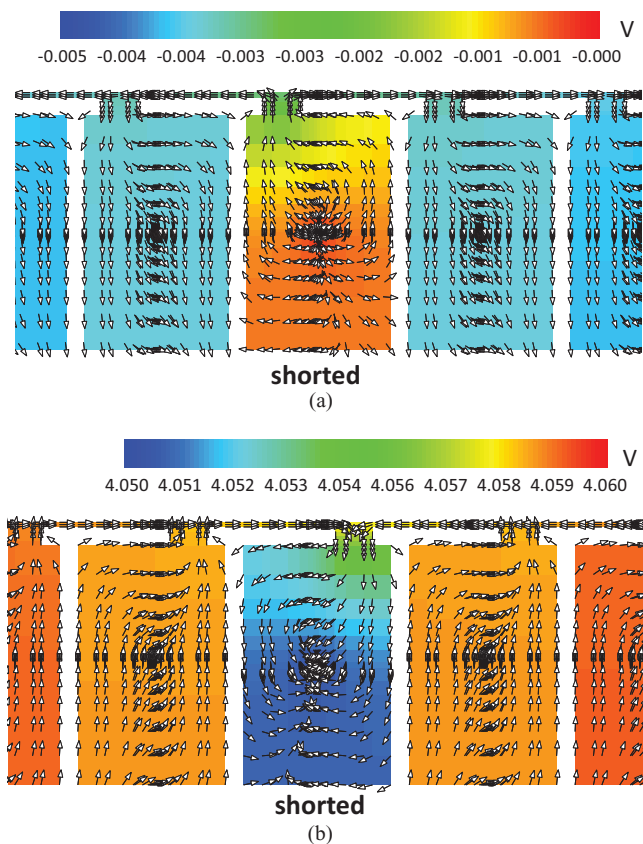


Figure 17. Solid potential and current flow vectors on the foils (shorted layer = 13th layer, $R_s = 4 \Omega/\text{layer}$) (a) Cu foil; (b) Al foil.

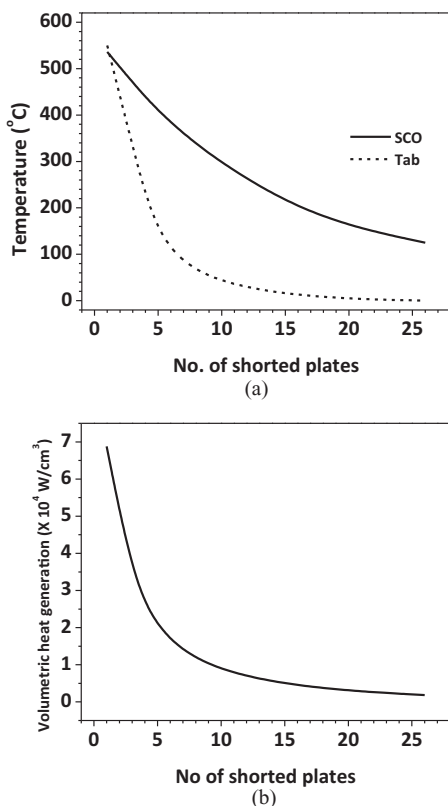


Figure 18. Effect of number of shorted layers ($R_s = 5.2 \text{ m}\Omega/\text{layer}$) (a) temperature rise of SCO and tab (b) volumetric heat generation on SCO.

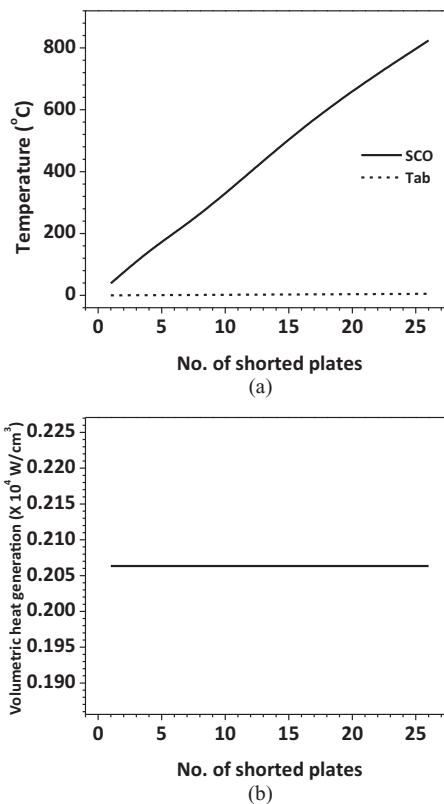


Figure 19. Effect of number of shorted layers ($R_s = 4 \Omega/\text{layer}$) (a) temperature rise of SCO and tab (b) volumetric heat generation on SCO.

to a reduced volumetric heat generation. Figure 18b shows that the volumetric heat generation in the SCO decreases significantly as the increase of shorted layer numbers. The significantly reduced volumetric heat generation is the reason for the lower temperature rise for multiple-layer shorting. Also noted from Figure 18a is the fact that the temperature rise of the tab reduces more rapidly than that of the SCO. This is because the tab has a much smaller thermal mass which makes its temperature more sensitive to the change of the heat generation.

Also, when more electrode layers are shorted, the shorting current will be more uniformly distributed. For example, as shown in Figure 20, when only one electrode layers is shorted, the shorting current contributed from the other 25 layers will all flow through the shorted layer. When three electrode layers are shorted, the shorting current coming from the other 23 layers will be evenly distributed to the three layers, each of which carries 1/3 of the current. When all 26 layers are shorted, each layer will carry the current generated in its own electrode. No current will be flowing among different electrode layers. Therefore, as the increase of shorted layer number, the heating mode will transition from local heating to global heating, as illustrated by the temperature contour in Figure 21.

For the large resistance case, the temperature rise as a function of shorted layer number exhibits the complete opposite trend. As shown in Figure 19a, the temperature rise of SCO increases with the number of shorted layer. The increasing rate is significant. For single-layer shorting, the temperature rise is only 39°C. But when all 26 layers are shorted, the temperature rise amounts to above 800°C, which will definitely trigger thermal runaway. This is because that when the shorting resistance is large, the shorting current is controlled by the shorting resistance rather than cell internal process. Increasing the number of shorted layers doesn't change the volumetric heat generation in SCO, as shown in Figure 19b. Instead, it creates heat generation spots in more electrode layers inside the cell. Because the heat dissipation area does not change and remains constant, the end result is the significantly increased temperature rise. The temperature contour in Figure 23

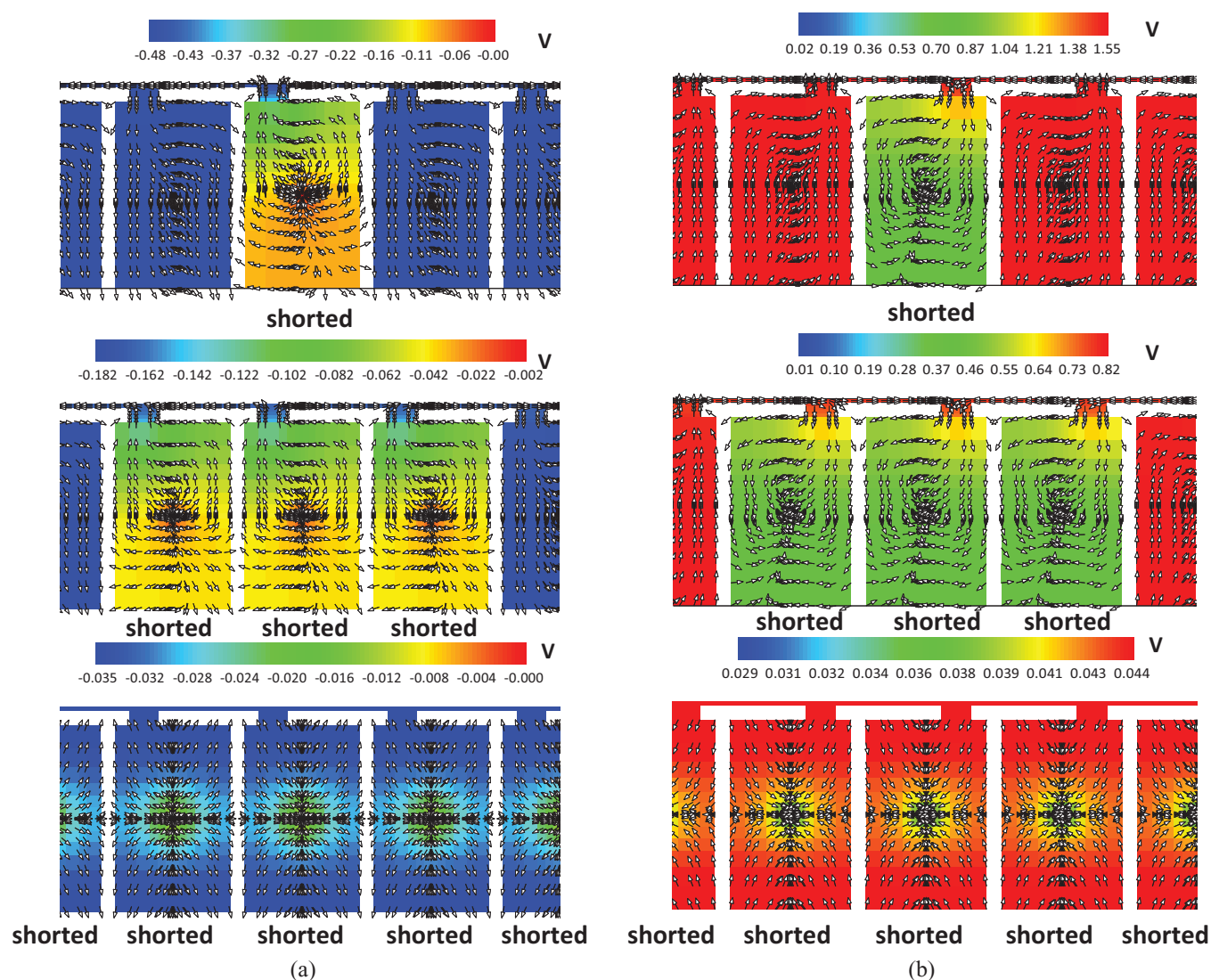


Figure 20. Solid potential and current flow vectors on the foils ($R_s = 5.2 \text{ m}\Omega/\text{layer}$) (a) Cu foil; (b) Al foil.

shows that regardless of the number of shorted layers, the heating is always localized in the SCO. The tab temperature rise in Figure 19a is very small compared with SCO temperature rise because of the very small heat generation on tabs. The current flow path is similar to that of small resistance case as shown in Figure 22, except that the voltage drop in the foils and tabs is much smaller than that of small resistance case, which indicates that most of the voltage drop and heat generation are concentrated in the SCO.

Conclusions

Internal short-circuit represents the most dangerous abusive condition for Li-ion batteries. Most of the field incidents involving Li-ion batteries were caused by internal short-circuits. In this chapter, a computational effort has been carried out to study the fundamental electrochemical and thermal mechanisms underlying the internal short-circuit process of a large-format Li-ion cell. The key conclusions derived from the simulation results are as follows.

Internal short-circuit process is very different from that simulated by nail penetration and crush tests. Internal short-circuit is usually caused by metal particle contamination during the manufacturing process or Li metal dendrite growth due to overcharge or degradation. The SCO causing the short-circuit is often very small so that only one

or a few electrode layers are shorted. In the nail penetration and crush tests, however, almost all of the electrode layers are shorted.

In the internal short circuit process, the shorted electrode layers where the SCO is located serve as the load to the other un-shortcd electrode layers. The current produced from the un-shortcd layers converges and flows through the tabs of the un-shortcd electrode layers. When the SCO resistance is small compared with the cell internal resistance, this will cause significant heating on the tabs. For large SCO resistance scenario, tab heating is negligible as the majority of heat generation is concentrated in the SCO. Therefore, for large format Li-ion cells, it is necessary to monitor the tab temperature in order to detect the occurrence of internal short-circuit.

Depending on the size of the SCO, one or multiple electrode layers can be shorted. The number of shorted electrode layers has a significant effect on the cell thermal response. For small SCO resistance, the temperature rise reduces dramatically as the increase of number of shorted electrode layer. For large SCO resistance case, however, the opposite trend is observed. The contradictory trends explain the poor reproducibility of the internal short-circuit experimental tests such as crush and nail penetration tests. In those tests, it is impossible to precisely control the shorting resistance and the number of shorted layers. The experimental results therefore vary significantly from test to test. New test methods which are designed to precisely control the shorting resistance and number of shorted electrode layers should be

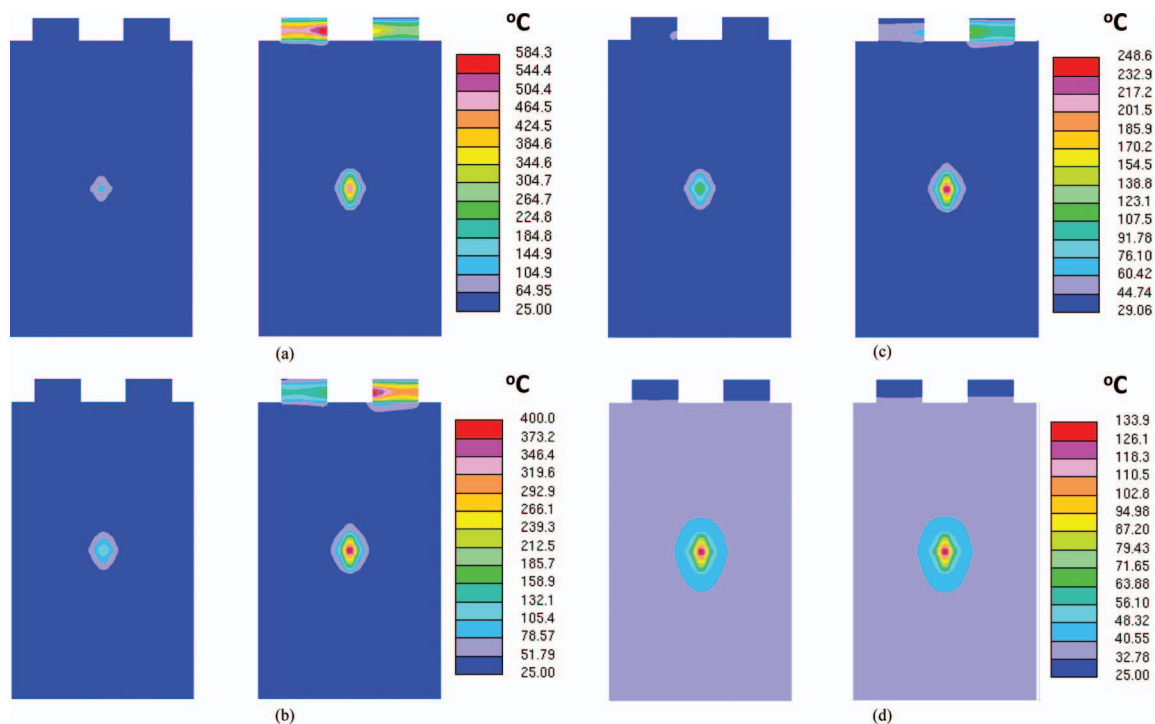


Figure 21. 2D temperature contours ($R_s = 5.2 \text{ m}\Omega$, left: cell surface, right: cell center plane, $t = 1 \text{ s}$) (a) 1 layer; (b) 5 layers; (c) 9 layers; (d) 26 layers.

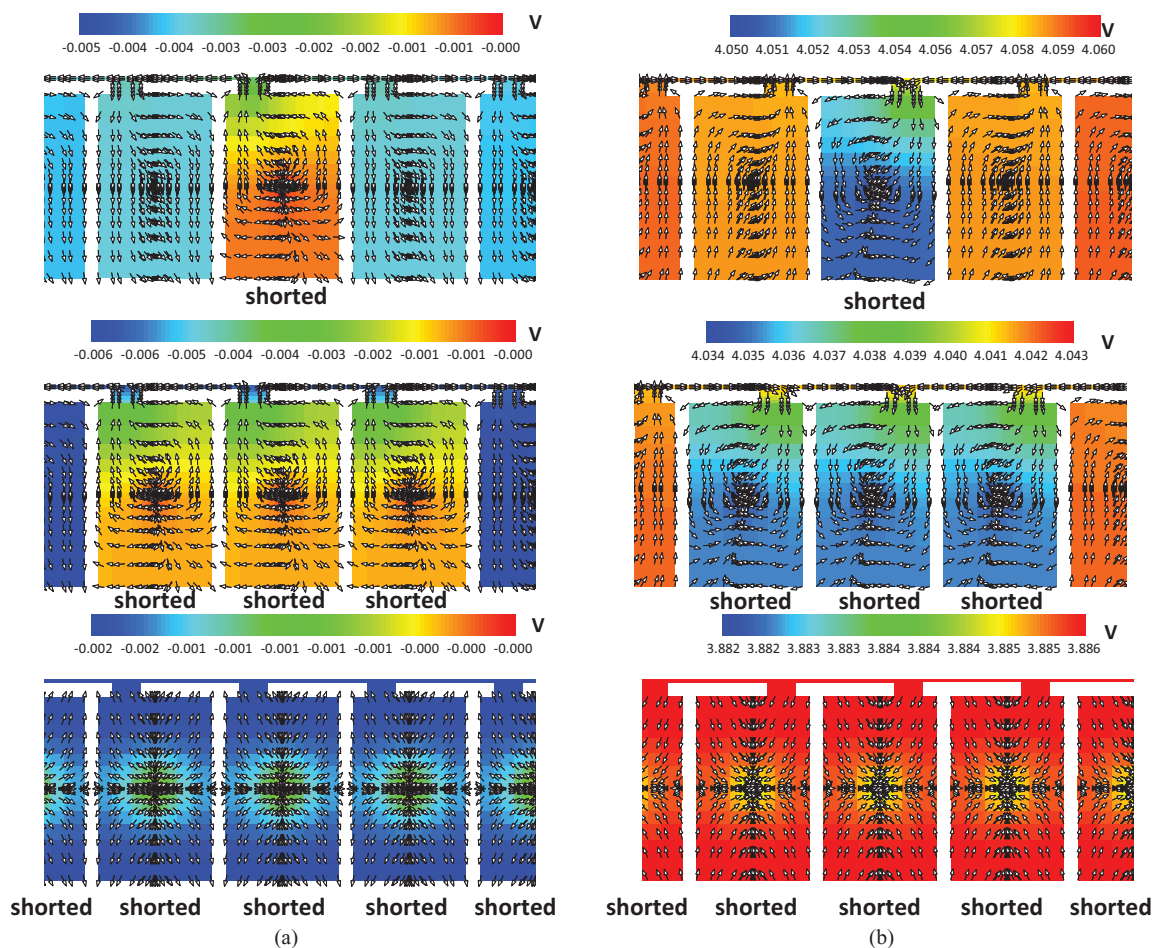


Figure 22. Solid potential and current flow vectors on the foils ($R_s = 4 \text{ }\Omega/\text{layer}$) (a) Cu foil; (b) Al foil.

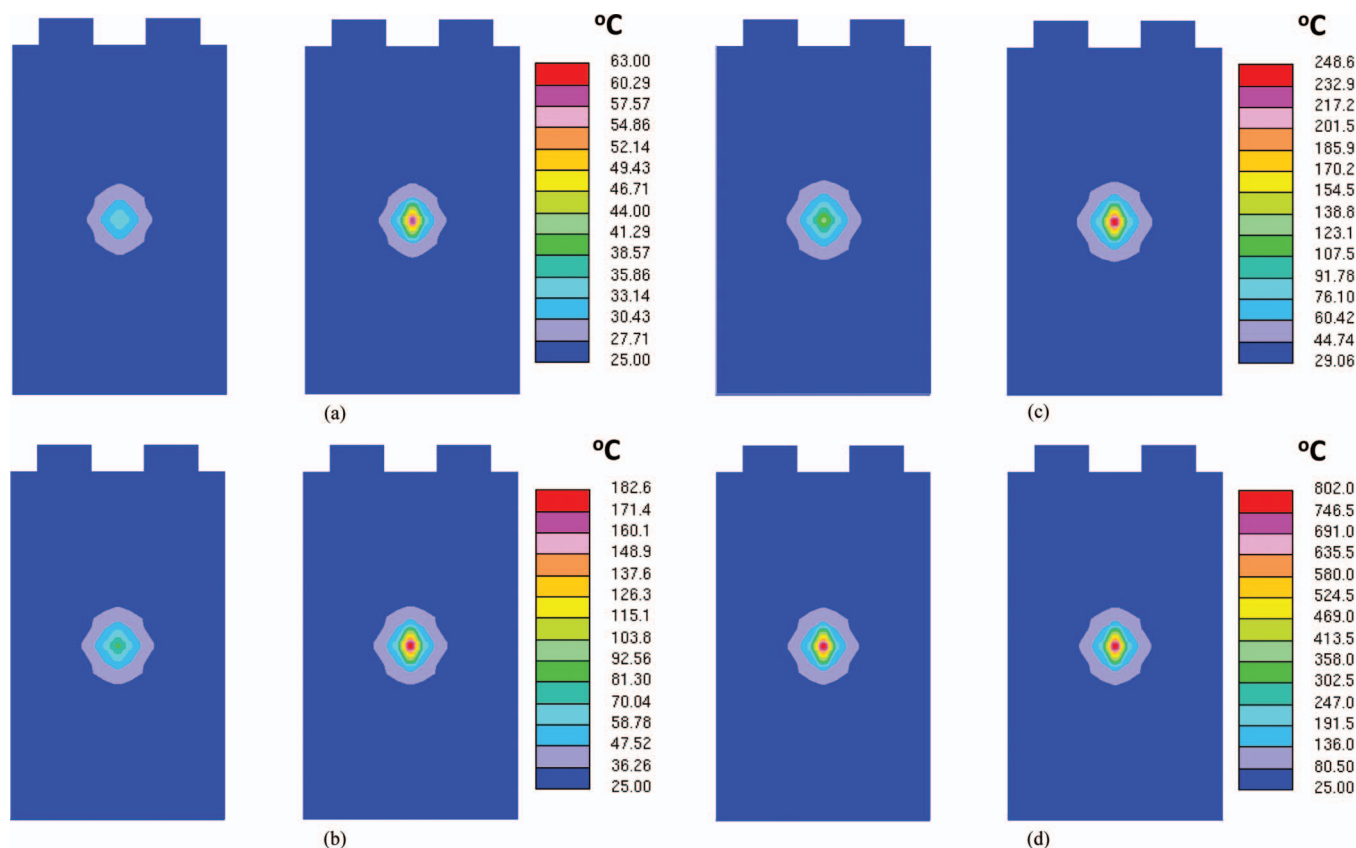


Figure 23. 2D temperature contours ($R_s = 4 \Omega/\text{layer}$, left: cell surface, right: cell center plane, $t = 10 \text{ s}$) (a) 1 layer; (b) 5 layers; (c) 9 layers; (d) 26 layers.

developed in order to quantify the safety behavior of Li-ion cells under internal short-circuit condition.

y coordinate along the electrode width, cm
 z coordinate along the electrode length, cm

Acknowledgments

Partial support of this work by DOE CAEBAT program is greatly acknowledged. We are grateful to EC Power for offering numerical algorithms and materials database through its AutoLion software and to Dr. Christian E. Shaffer for useful discussions.

List of Symbols

a_s	specific active surface area for an electrode, cm^2/cm^3
c	lithium concentration in phase, mol/cm^3
c_p	Specific heat capacity, $\text{J}/\text{kg K}$
D	diffusion coefficient of lithium species, cm^2/s
F	Faraday's constant, $96487 \text{ C}/\text{mol}$
f_{\pm}	mean molar activity coefficient of the electrolyte
h	heat transfer coefficient, $\text{W}/\text{cm}^2 \text{ K}$
I_s	shorting current, A
i_0	exchange current density, A/cm^2
j	volumetric reaction current, A/cm^3
k	rate constant for an electrode reaction
q	volumetric heat generation, W/cm^3
R	universal gas constant, $8.3143 \text{ J}/\text{mol K}$
R_s	shorting resistance, Ω
r	radial coordinate across a spherical particle, cm
T	temperature, $^{\circ}\text{C}$
T_{∞}	ambient temperature, $^{\circ}\text{C}$
t	time, s
t_+^0	transference number of lithium ion
U	equilibrium potential of an electrode reaction, V
x	coordinate along the electrode thickness, cm

Greek

α_a	anodic transfer coefficient
α_c	cathodic transfer coefficient
ε	volume fraction of a phase
ε_l	error of charge of balance
η	surface overpotential of an electrode reaction, V
κ	ionic conductivity of electrolyte, S/cm
κ_D	diffusional conductivity, A/cm
ρ	density, kg/cm^3
σ	electronic conductivity of an electrode, S/cm
ϕ	electrical potential in a phase, V

Subscripts

0	initial value
a	anode
c	cathode
e	electrolyte phase
s	solid phase

Superscripts

eff	effective
Li	lithium species

References

1. G. Girishkumar, B. McCloskey, A. Luntz, S. Swanson, and W. Wilcke, *J. Phys. Chem. Lett.*, **1**, 2193 (2010).
2. S.-i. Tobishima and J.-i. Yamaki, *J. Power Sources*, **81**, 882 (1999).
3. K. Ozawa, *Solid State Ionics*, **69**, 212 (1994).
4. M.-S. Wu, P.-C. J. Chiang, J.-C. Lin, and Y.-S. Jan, *Electrochimica acta*, **49**, 1803 (2004).
5. S.-i. Tobishima, K. Takei, Y. Sakurai, and J.-i. Yamaki, *J. Power Sources*, **90**, 188 (2000).
6. J. Nguyen and C. Taylor, in *Telecommunications Energy Conference, 2004. INTELEC 2004. 26th Annual International*, p. 146 (2004).
7. H. Maleki and J. N. Howard, *J. Power Sources*, **191**, 568 (2009).
8. M. Ichimura, in *Telecommunications Energy Conference, 2007. INTELEC 2007. 29th International*, p. 687 (2007).
9. T. Hatchard, D. MacNeil, A. Basu, and J. Dahn, *J. Electrochem. Soc.*, **148**, A755 (2001).
10. R. Spotnitz and J. Franklin, *J. Power Sources*, **113**, 81 (2003).
11. R. M. Spotnitz, J. Weaver, G. Yeduvaka, D. Doughty, and E. Roth, *J. Power Sources*, **163**, 1080 (2007).
12. G.-H. Kim, A. Pesaran, and R. Spotnitz, *J. Power Sources*, **170**, 476 (2007).
13. W. Zhao, G. Luo, and C.-Y. Wang, *J. Electrochem. Soc.*, **162**, A207 (2015).
14. T. Yamauchi, K. Mizushima, Y. Satoh, and S. Yamada, *J. Power Sources*, **136**, 99 (2004).
15. T. G. Zavalis, M. Behm, and G. Lindbergh, *J. Electrochem. Soc.*, **159**, A848 (2012).
16. S. Santhanagopalan, P. Ramadass, and J. Z. Zhang, *J. Power Sources*, **194**, 550 (2009).
17. W. Fang, P. Ramadass, and Z. J. Zhang, *J. Power Sources*, **248**, 1090 (2014).
18. G. Luo and C. Wang, *Chap. 6 in Lithium-Ion Batteries: Advanced Materials and Technologies*, in, CRC press (2011).
19. T. F. Fuller, M. Doyle, and J. Newman, *J. Electrochem. Soc.*, **141**, 982 (1994).
20. M. Doyle, T. F. Fuller, and J. Newman, *J. Electrochem. Soc.*, **140**, 1526 (1993).
21. M. Doyle, J. Newman, A. S. Gozdz, C. N. Schmutz, and J. M. Tarascon, *J. Electrochem. Soc.*, **143**, 1890 (1996).
22. W. Gu and C. Wang, *J. Electrochem. Soc.*, **147**, 2910 (2000).
23. V. Srinivasan and C. Wang, *J. Electrochem. Soc.*, **150**, A98 (2003).
24. K. Smith and C.-Y. Wang, *J. Power Sources*, **160**, 662 (2006).
25. W. Fang, O. J. Kwon, and C. Y. Wang, *Int. J. Energ. Res.*, **34**, 107 (2010).
26. Y. Ji, Y. Zhang, and C.-Y. Wang, *J. Electrochem. Soc.*, **160**, A636 (2013).
27. G. Zhang, C. E. Shaffer, C.-Y. Wang, and C. D. Rahn, *J. Electrochem. Soc.*, **160**, A610 (2013).
28. W. Zhao, G. Luo, and C.-Y. Wang, *J. Power Sources*, **257**, 70 (2014).
29. C. J. Orendorff, E. P. Roth, and G. Nagasubramanian, *J. Power Sources*, **196**, 6554 (2011).